THE JOURNAL OF PHYSICAL CHEMISTRY C

Article

pubs.acs.org/JPCC

Potential Paths for the Hydrogen-Bond Relaxing with $(H_2O)_N$ Cluster Size

Yongli Huang,[†,#] Xi Zhang,[‡,#] Zengsheng Ma,[†] Guanghui Zhou,[§] Yinyan Gong,[∥] and Chang Q Sun*[,⊥]

[†]Key Laboratory of Low-dimensional Materials and Application Technology (Ministry of Education) and Faculty of Materials Sciences and Engineering, Xiangtan University, Xiangtan 411105, China

[‡]Institute of Nanosurface Science and Engineering, Shenzhen University, Shenzhen 518060, China

[§]Department of Physics and Key Laboratory for Low-Dimensional Structures and Quantum Manipulation (Ministry of Education), Hunan Normal University, Changsha 410081, China

[∥]Institute for Coordination Bond Metrology and Engineering, College of Materials Science and Engineering, China Jiliang University, Hangzhou 310018, China

[⊥]NOVITAS, School of Electrical and Electronic Engineering, Nanyang Technological University, Singapore 639798, Singapore

ABSTRACT: Relaxation of the hydrogen bond (O:H−O) between oxygen ions of undercoordinated molecules fascinates the behavior of water nanodroplets and nanobubbles. However, probing such potentials remains yet far from reality. Here we show that the Lagrangian solution (Huang et al. *J. Phys. Chem. B* **2013**, *117*, 13639) transforms the observed H−O bond ($x = H$) and O:H nonbond ($x = L$) lengths and their characteristic phonon frequencies (d_x, ω_x) (Sun et al. *J. Phys. Chem. Lett.* **2013**, *4*, 2565) into their respective force constants and cohesive energies (k_x, E_x), which results in mapping of the potential paths for the O:H−O bond relaxing with $(H_2O)_N$ cluster size. Results show that molecular undercoordination not only reduces its size (H−O length d_H) with enhanced H−O energy from the bulk value of 3.97 to 5.10 eV for a H_2O monomer but also enlarges their separation (O:H distance d_L) with O:H energy reduction from 95 to 35 meV for a dimer. The H−O energy gain raises the melting point of water skin from the bulk value 273 to 310 K, and the O:H energy loss lowers the freezing temperature of a 1.4 nm sized droplet from the bulk value 258 to 202 K, which indicates droplet size induced dispersion of the quasisolid phase boundaries.

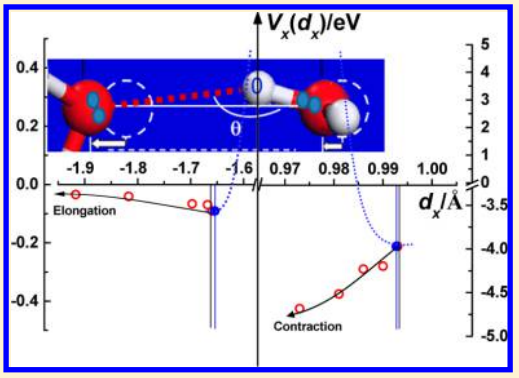

1. INTRODUCTION

As the source and central part of all lives, water and ice have attracted much attention because of their anomalous behavior when subjected to an external stimulus.[1−5] Undercoordinated water molecules that can be found at the edges of the hydrogen-bonded networks such as snowflakes, clouds, fogs, defects, bubbles, droplets, hydration shells, skins of bulk water, and ice are even more fascinating than those that are fully coordinated in the bulk.[6,7] For instance, water droplets encapsulated in hydrophobic nanopores[8,9] or ultrathin water films deposited on graphite, silica, and certain metals behave like ice, or called polywater, at room temperature. A monolayer of water melts at 325 K[10] compared to the skin of bulk water melting at 310 K.[6] The monolayer film of water at room temperature manifests "quasisolid" behavior and a hydrophobic nature that prevents it from being wetted itself by a water droplet.[11,12]

Molecular undercoordination elevated T_m is always coupled with depression of the homogeneous ice nucleation temperature (T_N). The T_N drops from the bulk value of 258[13] to 242 K for 4.4 nm sized droplets, 220 K for 3.4 nm sized droplets,[7] 205 K for 1.4 nm sized droplets,[14] and 172 K for 1.2 nm sized droplets.[15] Freezing transition for clusters containing 1−18 molecules cannot be observed at temperatures even down to 120 K.[16] Water and ice share the common supersolid skin[6] that is elastic, hydrophobic, less dense, and thermally more stable, which makes ice the most slippery and water skin the toughest ever known.

The skin O−O distance for water expands by at least 5.9%, compared to a 4.6% contraction for liquid methanol.[17] The skin bond contracts by up to 12% or even more for other normal substances.[18] The O−O distance in the skin and between a dimer is about 3.00 Å; the O−O distance in the bulk varies from 2.70[19] to 2.85 Å,[20] depending on experimental conditions. Besides, the volume of water confined in the 5.1 and 2.8 nm sized TiO_2 pores expands by 4% and 7.5%, respectively, with respect to bulk water.[21] The confined droplet forms the gel-like polywater. An extended tetrahedron containing two H_2O molecules unifies the density−geometry−size separation of molecules packed in water and ice, which defines the O−O

Received: April 24, 2015
Revised: June 26, 2015
Published: June 29, 2015

DOI: 10.1021/acs.jpcc.5b03921
J. Phys. Chem. C 2015, 119, 16962−16971

length of 2.6950 Å, O−H length of 1.6946 Å, and H−O bond length of 1.0004 Å at 4 °C for the tetrahedrally coordinated water molecules.[22]

Furthermore, molecular undercoordination imparts water local charge densification,[23−25] binding energy entrapment,[26−29] and nonbonding electron polarization.[24] For instance, the O 1s level shifts more deeply from the bulk value of 536.6 to 538.1 eV and to 539.7 eV when the bulk water is transformed into skin or into gaseous molecules.[30−32] An ultrafast liquid-jet UPS[24] resolved that the vertical bound energy (being equivalent to work function) for the solvated electrons changes from 3.3 eV when in the bulk interior to 1.6 eV when in the skin. The bound energy decreases further with the number N of the $(H_2O)_N$ clusters approaching to zero for isomers. Molecular undercoordination stiffens the H−O stretching phonon ω_H from the bulk value 3200 cm^{-1} to 3450 cm^{-1} for the skins of water and ice.[33−35] The ω_H shifts from 3200 to 3650 cm^{-1} when the N of the $(H_2O)_N$ cluster drops from 6 to 1 of the gaseous monomer.[36−41]

These entities make water nanodroplets and nanobubbles mechanically hardly destroyable and thermally much more stable than they are at the millimeter scale.[42,43] What is the difference between the undercoordinated water molecules and those fully coordinated in the bulk? Why do the O 1s binding energy and the O:H−O phonon frequencies change with molecular cluster size? Why are droplets and bubbles mechanically stronger and thermally more stable?

The inter- and intramolecular interactions between undercoordinated water molecules and the associated electronics, energetics, and phononics could be crucial to these observations. Therefore, it is indispensable to explore the potential paths for the segmented O:H−O bond relaxing with $(H_2O)_N$ size. However, quantitative information about the evolution of these potentials, particularly for interaction between undercoordinated water molecules, and their indication to the anomalies of water droplets and bubbles at the nanometer scale remain unresolved.

Teixeira[44] suggested in 1998 that a symmetric double-well potential exists between neighboring O ions to accommodate the hydrogen proton "frustrating"[45] between these two wells. When the O ions are forced closer, the pairing potential wells turn into single located midway between O ions. In 2004, Wernet et al.[46] hypothesized instead the existence of an asymmetric H-bonding potential which Soper[47] further investigated by assuming different charges on hydrogen protons in order to create this asymmetry and examine whether that could be supported by diffraction data. Considerable efforts have also been made since then by many researchers[48−51] toward formulating and quantifying such asymmetric potentials.

Anomalies due to molecular undercoordination are beyond the scope of currently available models including the nonrigid water potential[52] though some recent experimental and theoretical studies have revealed covalent characteristics of the hydrogen bonding.[53−55] Tremendous work has been done on the phonon relaxation dynamics using neutron, Raman, and infrared absorption methods under various conditions.[56−58] However, the state-of-the-art techniques, including X-ray and neutron diffraction and electron and phonon spectroscopies could hardly prove this hypothesis as these techniques could not directly detect such local and short-range potentials.

With the aid of phonon spectrometrics and quantum computations using density functional theory (DFT)[59] and molecular dynamics (MD)[60] methods, we have resolved, from the perspective of O:H−O bond cooperativity,[18] multiple issues demonstrated by compressed ice,[61,62] by cooled water and ice,[13,63] by salted water,[64] and by undercoordinated molecules.[6,65] These anomalies include the Mpemba paradox (hot water freezes faster),[63] the Hofmeister effect (NaCl modulates the surface tension and the phonon frequencies of its solution),[64] floating of ice (density anomaly),[13] slipperiness of ice (supersolid skin),[6] proton centralization in ice phase X and low compressibility of ice,[61] water's tough skin (supersolid skin),[6] etc. Progress made insofar has formed the subjects of recent treatises[1,66] for more details.

We have demonstrated that the Lagrangian oscillating dynamics could be insofar most efficient[62] to deal with the hydrogen bond (O:H−O) relaxation dynamics in the strongly correlated and fluctuating water ice system. This strategy has transformed the known O:H ($x = L$) and H−O ($x = H$) segmental length and stretching vibration frequency (d_x, ω_x) into their force constants and bond energies (k_x, E_x) of the O:H−O bond at each equilibrium as a function of pressure.[62] A further extension of the practice could lead to mapping the potential paths for the O:H−O bond relaxing with cluster size with the due relaxation of the O:H−O bond in length and vibration frequencies as a function of cluster size.[62,65] Observations provide insight into the physical mechanism for the unusual thermodynamic behavior, melting point elevation, and freezing point depression of water nanodroplets and nanobelts from the perspective of undercoordination dispersed quasisolid phase boundaries.

2. PRINCIPLES

2.1. O:H−O Bond Potential Functions. The hydrogen bond, $O^{2\delta-}$:$H^{\delta+}$−$O^{2\delta-}$ ($\delta < 1$; for simplicity in discussion, we take $\delta < 1$ and omit the valence sign convention), consists of the intermolecular O:H nonbond and the intramolecular H−O polar covalent bond rather than either of them alone. The ":" is the electron lone pair of oxygen, and the "−" represents the bonding pair shared by O and H ions. We considered a quasi-linear O:H−O bond geometry for simplicity because the ∠O:H−O containing angle is largely irrelevant to the physical properties such as the O 1s core level shift and phase transition temperatures.[13]

By averaging the surrounding background of long-range interactions of H_2O molecules, protons, and the nuclear quantum effect on fluctuations,[67,68] we focused on the short-range interactions in a O:H−O bond with the H atom being taken as the coordination origin. The short-range interactions include the Lennard-Jones (L-J) potential limited to the O:H nonbond, the exchange interaction to the H−O polar-covalent bond, and the Coulomb repulsion between the lone and the shared electron pairs attached to adjacent oxygen ions

DOI: 10.1021/acs.jpcc.5b03921
J. Phys. Chem. C 2015, 119, 16962−16971

$$\begin{cases} V_L(r_L) = V_{L0}\left[\left(\frac{d_{L0}}{r_L}\right)^{12} - 2\left(\frac{d_{L0}}{r_L}\right)^{6}\right] & \text{(O:H; L-J potential } (V_{L0}, d_{L0})) \\ V_H(r_H) = V_{H0}[e^{-2\alpha(r_H - d_{H0})} - 2e^{-\alpha(r_H - d_{H0})}] & \text{(H−O; Morse potential } (\alpha, V_{H0}, d_{H0})) \\ V_C(r_C) = \frac{q_O^2}{4\pi\varepsilon_r\varepsilon_0 r_C} & \text{(O−O; Coulomb potential } (q_O, \varepsilon, r_C)) \end{cases} \quad (1)$$

where V_{L0} and V_{H0}, commonly denoted E_{L0} and E_{H0}, are the potential well depths, or bond energies, of the respective segment. The r_x (x = L, H, and C) denotes the interionic distances (corresponding to the length of the springs in Figure 1) at arbitrary position, and the d_{x0} is at the equilibrium point

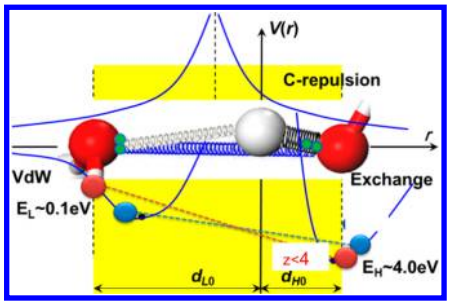

Figure 1. Schematic illustration of the segmented O:H−O bond with springs representing the short-range interactions with the H atom being the coordination origin. The intramolecular exchange interaction is limited to the H−O bond (H, right-hand side). The intermolecular van der Waals like (vdW-like) force is limited to the O:H nonbond (L, left-hand side). The interelectron-pair Coulomb repulsion (C-repulsion) force is limited to the region of O−O. The pair of dots on oxygen (large green dot) in the left denotes the electron lone pair, and the pair of dots on the right denotes the bonding pair. The Coulomb repulsion pushes both O ions away from their ideal equilibrium positions. Molecular undercoordination shortens and stiffens the H−O bond and meanwhile lengthens and weakens the O:H nonbond, as indicated by $z < 4$.[65]

without the involvement of Coulomb repulsion. The α parameter determines the width of the potential well. ε_r is the relative dielectric constant of bulk ice. ε_0 is the vacuum dielectric constant. The q_O denotes the net charge on oxygen ions. A sum term of all long-range interactions of the neighboring H protons or O ions is averaged as the background.

We are concerned more about the equilibrium coordinates of bond length and bond energy (d_x, E_x) than the shape of the potentials. Because of the short-range nature of the interactions, only the solid lines in the shaded area for the basic O:H−O unit in Figure 1 are effective. One must switch off a particular potential and on the other immediately once moves to the boundary of the region or across the atomic site. The O:H cohesive energy at the 0.1 eV level is about 3% of 4.0 eV for the H−O bond, which is within the error tolerance but plays the key role in determining the anomalies of water and ice. Spatial decay of any potential is strictly forbidden in the irrespective regime across. Under external excitation, the shape of the potentials may remain but the equilibrium coordinates (d_x, E_x) must vary with the stimulus applied.

2.2. Lagrangian Oscillating Dynamics.

The segmented O:H−O bond performs as an asymmetric oscillator pair coupled by the Coulomb interaction and bridged by the H atom at the fixed coordination origin.[1] The reduced mass of the (H_2O):(H_2O) oscillator is $m_L = 18 \times 18/(18 + 18)m_0 = 9m_0$, and that of the H−O oscillator is $m_H = 1 \times 16/(1 + 16)m_0 = 16/17m_0$ with m_0 being the unit proton mass of 1.66×10^{-27} kg. The motion of the asymmetric, coupled O:H−O oscillator pair follows the Lagrangian equation[62]

$$\frac{d}{dt}\left(\frac{\partial L}{\partial(dq_i/dt)}\right) - \frac{\partial L}{\partial q_i} = Q_i \quad (2)$$

The Lagrangian $L = T - V$ consists of the total kinetic energy T and the total potential energy V. Q_i is the generalized nonconservative force. Here, it is the force due to the undercoordination effect f_z (molecular undercoordination shortens and stiffens the H−O bond spontaneously, which lengthens and softens the O:H nonbond through Coulomb repulsion.[65] The time-dependent $q_i(t) = u_x$ represents the generalized variables, denoting the coordinates of O atoms in the O:H−O bond represented by the x springs. The kinetic energy T consists of two terms, as the H is fixed at the coordination origin

$$T = \frac{1}{2}\left[m_L\left(\frac{du_L}{dt}\right)^2 + m_H\left(\frac{du_H}{dt}\right)^2\right] \quad (3)$$

The potential energy V is composed of three terms given in eq 1: the vdW-like L-J interaction V_L (u_L), the exchange interaction V_H (u_H), and the Coulomb repulsion $V_C(u_C) = V_C(u_H - u_L)$.We took the u_x as the coordinates and d_x as the segmental length. Therefore, $d_{C0} = -u_{L0} + u_{H0}$ is the nearest O−O distance at equilibrium without Coulomb repulsion involvement. The $d_C = -u_L + u_H$ is the O−O distance with Coulomb repulsion involvement. The O atom dislocates from the equilibrium to another equilibrium by $\Delta_x = u_x - u_{x0}$ upon the Coulomb repulsion being involved. A harmonic approximation of these potentials at each equilibrium by omitting the higher-order terms in their Taylor's series yields

$$\begin{aligned} V &= V_L(u_L) + V_H(u_H) + V_C(u_H - u_L) \\ &\approx [V_L(u_{L0}) + V_H(u_{H0}) + V_C(u_C)] - V_C'\Delta u_C \\ &\quad + \frac{1}{2}[k_L\Delta u_L^2 + k_H\Delta u_H^2 + k_C\Delta u_C^2] \end{aligned} \quad (4)$$

where $V_x(u_{x0})$ is the potential well depths ($n = 0$ terms) of the respective bond, and Δu_x is the amplitude of vibration. Noting that the Coulomb potential is out of equilibrium and that the repulsion force is always positive, one can then expand these potentials at their equilibrium based on harmonic approx-

DOI: 10.1021/acs.jpcc.5b03921
J. Phys. Chem. C 2015, 119, 16962−16971

imation, which ensures sufficient accuracy of the elucidated potential paths.[62]

In the Taylor series, the terms of $n = 1$ equal zero at equilibrium, $V'_x(u_{x0}) = 0$, without Coulomb repulsion; $V'_x(u_x) + V'_C(u_C) = 0$, with Coulomb repulsion; $V'_x(u_x) + V'_C(u_C) + f_z = 0$, with an addition of the molecular undercoordination effect ($z < 4$). Here $V'_C \neq 0$ denotes the first-order derivative of the Coulomb potential at the equilibrium due to the sum $V'_x(u_x) + V'_C(u_C) = 0$. Terms of $n = 2$, or the potential curvatures, denote the force constants, i.e., $k_x = V'' = d^2V_x/du_x^2|_{u_{x0}}$ for harmonic oscillators. Terms of $n \geq 3$ are insignificant and negligible, which is adequate for seeking the nature and trend of the potential paths. The involvement of the Coulomb repulsion dislocates both O ions slightly outwardly by Δ_x from their respective initial equilibrium, shifting the atomic distance from d_{x0} to $d_x = d_{x0} + \Delta_x$. The Coulomb repulsion raises the respective potential well depths from E_{x0} to E_x by the same amount as both oxygen ions are subject to the same repulsive force.

Substituting eqs 3 and 4 into eq 2 yields the coupled motion equations for the O:H−O oscillator pair,

$$\begin{cases} m_L \dfrac{d^2u_L}{dt^2} + (k_L + k_C)u_L - k_C u_H + k_C(\Delta_L - \Delta_H) \\ \quad - V'_C - f_z = 0 \\ m_H \dfrac{d^2u_H}{dt^2} + (k_H + k_C)u_H - k_C u_L - k_C(\Delta_L - \Delta_H) \\ \quad + V'_C + f_z = 0 \end{cases} \tag{5}$$

2.3. Analytical Solutions. *2.3.1. General Solution.* A Laplace transformation of the Lagrangian turns out the following

$$\begin{cases} u_L = \dfrac{A_L}{\gamma_L} \sin \gamma_L t + \dfrac{B_L}{\gamma_H} \sin \gamma_H t \\ u_H = \dfrac{A_H}{\gamma_L} \sin \gamma_L t + \dfrac{B_H}{\gamma_H} \sin \gamma_H t \end{cases} \tag{6}$$

The coefficient denotes the vibrational amplitude of the respective segment. γ_x is the angular frequency of the x oscillator, which depends on the force constant and the reduced mass of the oscillating dimer. The O:H and the H−O segments share the same form of eigenvalues of stretching vibration. The following correlates the k_x and the ω_x

$$k_{H,L} = 2\pi^2 m_{H,L} c^2(\omega_L^2 + \omega_H^2) - k_C \pm \sqrt{[2\pi^2 m_{H,L} c^2(\omega_L^2 - \omega_H^2)]^2 - m_{H,L} k_C^2 / m_{L,H}} \tag{7}$$

where c is the velocity of light traveling in vacuum. Omitting the Coulomb repulsion will degenerate the coupled oscillators into the isolated (H_2O):(H_2O) and H−O oscillators with respective vibration frequency of $\omega_x = (2\pi c)^{-1}(k_x/m_x)^{1/2}$.

2.3.2. Specific Solution. Given the frequency ω_x and the force constant k_C of Coulomb repulsion, one can obtain the force constant k_x, the potential well depth E_{x0}, and the binding energy E_x, at each equilibrium of these two segments during relaxation. The force constant due to Coulomb repulsion is $k_C = q_O^2/(2\pi\varepsilon_r\varepsilon_0 d_C^3) = 0.17$ eV/Å^2 at equilibrium by taking $\varepsilon_0 = 8.85 \times 10^{-12}$ F/m for vacuum, $\varepsilon_r = 3.2$ for ice, and $q_O = 0.652$ e for the undercoordinated skin molecules, as optimized using DFT calculations.[6]

Calculations[62] showed that the $k_x(\omega_x)$ changes with the respective segmental vibration frequency ω_x. The terms of the $k_L(\omega_H)$ and the $k_H(\omega_L)$ remain, however, almost constant. Therefore, eq 7 simplifies into the expression for the coupled oscillators

$$\omega_x = (2\pi c)^{-1} \sqrt{\frac{k_x + k_C}{m_x}} \tag{8}$$

Table 1 shows the procedure of derivatives and the outcome with known (d_x, ω_x) as input. For instance, at equilibrium,

Table 1. Derivatives of the L-J and Morse Potentials at Equilibrium and at Each Quasiequilibrium Position, Which Transits the Known (d_x, ω_x) into the (k_x, E_x)

derivatives	O:H potential	H−O potential	outcome
$V_x'(u_{x0}) = 0$	-		E_{x0}
$V_x'(u_x) + V_c'(u_C) = 0$	-		E_x, u_x
$V_x'' = k_x(k_C\omega_x)$	$72E_{L0}/d_{L0}^2$	$2\alpha^2 E_{H0}$	α
V_x'''	$-1512E_{L0}/d_{L0}^3$	$-6\alpha^3 E_{H0}$	-

$V_x'(u_{x0}) = 0$ defines the E_{x0} and d_{x0}; $V_x'(u_x) + V_C'(u_C) = 0$ defines the E_x. The difference between E_x and E_{x0} is the Coulomb repulsion energy E_C. Likewise, $V_x'' = k_x$ and $V_x'' + V_C'' = k_x + k_C$ (see eq 8). The known k_C and ω_x define the V_x'' value and parameters involved in the respective potential function, given in eq 1.

With the derived values of $k_L = 2.39$ eV/Å^2, $k_H = 36.09$ eV/Å^2, and the known $E_H = 3.97$ eV and $E_L = 0.095$ eV, we can determine all the parameters in the L-J and the Morse potentials, as well as the force fields of the O:H−O bond at the ambient

$$\begin{cases} k_L = 72E_{L0}/d_{L0}^2 = 2.39 \text{ eV/A}^2 \\ k_H = 2\alpha^2 E_{H0} = 36.09 \text{ eV/A}^2 \end{cases}$$

or

$$\begin{cases} E_{L0} = 2.39 \times 1.654^2/72 = 0.091 \text{ eV} \\ \alpha = (36.09/3.97/2)^{1/2} = 2.13 \text{ A}^{-1} \end{cases} \tag{9}$$

With the known Coulomb potential, the computed segmental d_x and ω_x functions of $(H_2O)_N$,[65] one can obtain parameters in the L-J (E_{L0}, d_{L0}) and the Morse (E_{H0}, α) potentials, as illustrated in Table 1. The E_L may have different values subjecting to experimental conditions or approaching methods. For instance, the E_L varies from 0.05 eV for ice at zero pressure to 0.25 eV at 40 GPa and turns to 0.16 eV at 60 GPa pressure.[62] It is therefore meaningful to consider the E_x values associated with experimental conditions. The currently used $E_H = 3.97$ eV was obtained by fitting the T_C−P profiles for both ice VII−VIII phase transition and ice melting and the $E_L = 0.095$ eV by fitting to the temperature dependence of the water surface tension.[1]

Given the $\omega_L = 218$ cm^{-1} and $\omega_H = 3225$ cm^{-1} for the $(H_2O)_6$ cluster[65] and the known k_C, eq 8 yields $k_L = 2.39$ eV/Å^2 and $k_H = 36.09$ eV/Å^2. With the known $d_L = 1.659$ Å and $d_H = 0.993$ Å, under Coulomb repulsion, one can obtain the length u_{L0} of −1.654 Å and the u_{H0} of 0.9927 Å at equilibrium. Coulomb repulsion lengthens the O−O distance by 0.0053 Å from 2.6467 to 2.6520 Å, according to the equilibrium conditions with and without Coulomb repulsion involvement.

DOI: 10.1021/acs.jpcc.5b03921
J. Phys. Chem. C 2015, 119, 16962−16971

Table 2. N Dependence of the Energetics at Different Order of Differentials As a Function of $(H_2O)_N$ Size[a]

	E_x (eV)					
	O:H potential $V_L(r)$			H−O potential $V_H(r)$		
N	0th (10^{-3})	2nd (10^{-5})	3rd (10^{-6})	0th	2nd (10^{-6})	3rd (10^{-10})
6	90.73	2.45	0.47	3.97	1.62	0.10
5	69.42	3.20	0.80	4.19	1.51	9.03
4	66.16	3.35	0.88	4.25	1.43	8.27
3	40.59	5.27	2.21	4.65	1.10	5.29
2	34.66	6.02	2.93	4.79	0.94	4.09

[a]Both the O:H nonbond and H−O bond are insensitive to the higher-order derivatives.

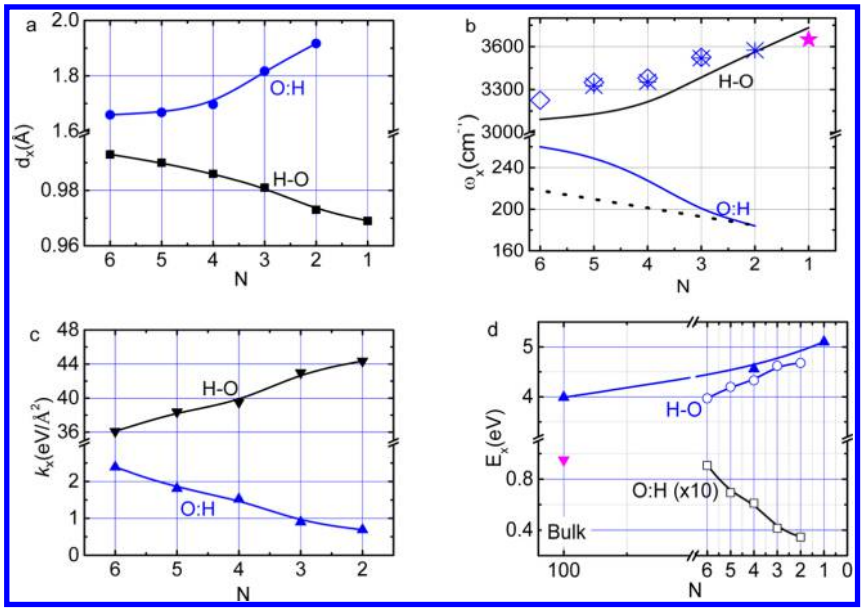

Figure 2. Cluster size (N) dependence of the segmental (a) length d_x, (b) phonon frequency ω_x, (c) force constant k_x, and (d) cohesive energy E_x of the O:H−O bond in $(H_2O)_N$ clusters.[65] Scattered data in (b) are measurements.[36−38,41]The broken line in (b) modifies the calculation ω_L with respect to that, 220 cm^{-1}, for bulk water and to that the calculated ω_H matches the measured value at N = 2. Solid triangles in (d) are measured E_L for the bulk (0.095 eV),[69] and E_H are measurements from bulk (3.97 eV),[6] skin (4.66 eV),[1] and gaseous monomers (5.10 eV).[70]

Table 3. DFT-Derived Segmental Length d_x, ∠O:H−O Containing Angle θ, and Phonon Frequency ω_x for $(H_2O)_N$ Clusters[65a]

	monomer	dimer	trimer	tetramer	pentamer	hexamer	bulk[13]
N	1	2	3	4	5	6	Ih
d_H (Å)	0.969	0.973	0.981	0.986	0.987	0.993	1.010
d_L (Å)	-	1.917	1.817	1.697	1.668	1.659	1.742
θ (deg)	-	163.6	153.4	169.3	177.3	168.6	170.0
ω_L (cm^{-1})	-	184	198	229	251	260	-
ω_L (cm^{-1})	-	184	190	200	210	218	220
ω_H (cm^{-1})	3732	3565	3387	3194	3122	3091	-
ω_H (cm^{-1})[50−52,55]	3650	3575	3525	3380	3350	3225	3150
Θ_{DL} (K)	-	167	171	180	189	196	198[69]
Θ_{DH} (K)	3650	3575	3525	3380	3350	3225	3150
T_N (K)	-	94	110	180	188	246	258
T_m (K)	-	322	318	291	289	273	273

[a]Presented are also N dependence of the Debye temperatures Θ_{Dx}, freezing temperature T_N, and melting point T_m estimated herewith. Indicates the corrected ω_L as captioned in Figure 2[b]. [b]Experimentally observed T_m elevation and T_N depression: T_m = 325 K (monolayer);[10] 310 K (skin of bulk).[6] T_N = 242 K (4.4 nm droplet);[7] 220 K (3.4 nm droplet);[7] 205 K (1.4 nm droplet);[14] 172 K (1.2 nm droplet);[15] <120 K (1−18 molecules).[16]

These values may be subject to accuracy due to the artifact in the calculation algorithm and limitation of available probing techniques. However, these values do reflect the nature origin and the general trend of the segmental relaxation under Coulomb repulsion and molecular undercoordination, which dominate the performance of water ice at the nanometer scale.

3. LOCAL POTENTIAL PATHS FOR THE RELAXED O:H−O BOND

3.1. Accuracy and Reliability. Table 2 lists the zeroth, the first, the second, and the third derivatives of the Taylor series as a function of $(H_2O)_N$ cluster size. For both the O:H nonbond and the H−O bond, the contribution of the high-order terms to

DOI: 10.1021/acs.jpcc.5b03921
J. Phys. Chem. C 2015, 119, 16962−16971

the respective binding energy is negligibly small. Therefore, the harmonious approximation at each equilibrium site is valid in the first-order approximation for the nature origin and the trend of variation.

3.2. *N*-Dependent d_x, ω_x, k_x, and E_x. Figure 2a,b and Table 3 featured the N dependence of the d_x and ω_x values obtained using DFT computations.[65] The present analytical solution transforms these eluded d_x and ω_x into the force constant and bond energy (k_x, E_x) of the respective segment of the O:H−O bond, from one equilibrium to another, as the N is reduced. This transformation results in mapping the potential paths for the O:H−O bond at relaxation (see results featured in Table 4 and Figure 2c,d). The counters of the equilibrium points follow the forms of the respective potentials, as given in eq 1. Therefore, one has to consider the relaxation of the bond potentials when the object is subject to stimulus, instead of keeping the potentials at fixed equilibria.

Table 4. N Dependence of the (k_x, E_x, Δ_x) for the O:H−O Bond in $(H_2O)_N$ Clusters[a]

N	E_L (meV)	E_H (eV)	k_L (eV/Å^2)	k_H (eV/Å^2)	Δ_L (10^{-3} Å)	Δ_H (10^{-4} Å)
6	90.70	3.97	2.39	36.09	4.53	2.99
5	69.39	4.20	1.81	38.39	5.95	2.80
4	66.13	4.23	1.67	39.01	6.34	2.71
3	40.54	4.62	0.90	42.99	10.84	2.26
2	34.60	4.68	0.69	44.35	13.23	2.05

[a]The O:H relaxation (Δ_L) is more significant that the H−O bond (Δ_H) from one N value to the next.

MD calculations[6] suggested that the H−O bond contracts from the bulk value of ∼1.00 to ∼0.95 at the skin, which is associated with O:H elongation from ∼1.68 to ∼1.90 Å with high fluctuation. This cooperative relaxation results in a 6.8% d_{OO} elongation or a 13% density loss of the skin. The measured d_{OO} of 2.965 Å[17] yields the lengths of d_H = 0.8406 Å and d_L = 2.1126 Å, which turns out a 0.75 g·cm^{-3} skin mass density. Consistency between these observations and the current Lagrangian transformation reveals the true situation of the O:H−O bond relaxation and the associated mass density and their correlation with the O:H−O bond potential paths varying with molecular undercoordination.

3.3. Potential Paths. Figure 3 shows the evolution of the O:H−O bond potential paths with $(H_2O)_N$ size, which agrees with experimental results (Figure 2d). At N = 6, O atoms dislocate from the equilibrium (blue dots) outwardly by different amounts with identical energy elevation once the Coulomb repulsion is involved. When the N reduces from 6 to 2, the H−O bond contracts from 0.993 to 0.973 Å, and its cohesive energy shifts from 3.97 to 4.68 eV, agreeing with the changing trend from bulk (3.97 eV) to the skin (4.66 eV) and to the monomer in the gaseous phase (5.10 eV).[70] The O:H expands from 1.659 to 1.917 Å, and the energy shifts from 90.70 to 34.60 meV, compared with the bulk value of 95 meV.[69] These values may be subject to accuracy, as the DFT calculations are algorithm sensitive.[65] Compared is the O:H−O potential path for compressed ice, which takes the opposite trend of cluster size reduction.[62]

4. THERMODYNAMICS OF UNDERCOORDINATED WATER MOLECULES

4.1. T_m Elevation and T_N Depression. The droplet-size effect on T_m and T_N is often referred to as "superheating" at melting and "supercooling" at freezing. Supercooling, also known as undercooling, is the process of lowering the temperature of a liquid or a gas below its freezing point without it becoming a solid.[71] Superheating is the opposite. Supercooled water occurs in the form of small droplets in clouds and plays a key role in the processing of solar and terrestrial radiative energy fluxes. Supercooled water is also important for life at subfreezing conditions for the commercial preservation of proteins and cells and for the prevention of hydrate formation in nature gas pipelines. In fact, T_m elevation is different from "superheating, and T_N depression is different from "supercooling". The former is intrinsic, and the latter is process dependent.

Generally, melting a specific atom inside a normal substance requires heat that is a fraction of its cohesive energy, $E_C = zE_z$, i.e., the sum of bond energy E_z over its coordination neighbors (z or CN). The T_m of a solid changes with the solid size because of the skin atomic undercoordination and the varied fraction of undercoordinated atoms in the skin.[18] However, for water and ice, the presence of the critical temperatures at 273 K (T_m) and 258 K (T_N),[13] for transiting the bulk liquid into the quasisolid and then into solid, indicates that a quasisolid (or quasiliquid) phase exists in this temperature regime. However, the quasisolid phase is absent from the existing phase diagram of water and ice.

Why and how does droplet size affect the T_m and the T_N?

4.2. O:H−O Bond Specific Heat Disparity. First, one has to consider the specific heat per bond $\eta(T/\Theta_D)$ in Debye

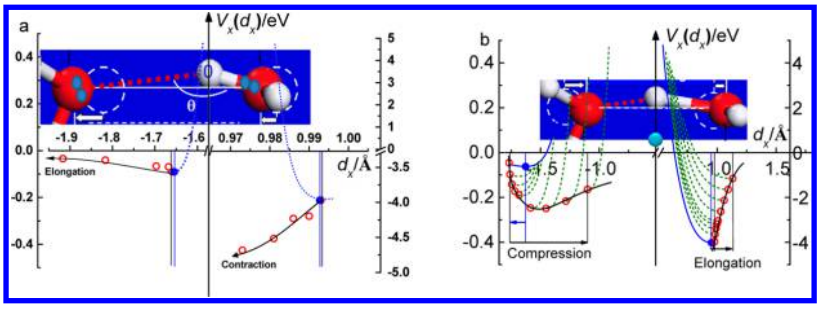

Figure 3. Potential paths (red circles) for the O:H−O bond relaxing with (a) $(H_2O)_N$ cluster size N (r. to l.: N = 6, 5, 4, 3, 2) and (b) pressure (r. to l.: P = 0, 5, 10, 15, 20, 30, 40, 50, 60 GPa).[62] Blue dots are the equilibrium without interoxygen Coulomb repulsion, $V'_x = 0$. Red circles in the (a) rightmost and (b) leftmost are in the equilibrium, $V'_x + V'_C = 0$, and the rest meets $V'_x + V'_C + f_{ex} = 0$. The f_{ex} is the hidden force due to stimulus. Results indicate (a) that molecular undercoordination reduces the H_2O size (d_H) but increases their separations (d_L) with H−O bond stiffening and O:H nonbond softening. Compression has the opposite effect to molecular undercoordination on O:H−O bond relaxation.

DOI: 10.1021/acs.jpcc.5b03921
J. Phys. Chem. C 2015, 119, 16962−16971

approximation when dealing with the thermodynamic behavior of a substance from the atomistic point of view. The specific heat is regarded as a macroscopic quantity integrated over all bonds of the specimen, which is also the amount of energy required to raise the temperature of the substance by 1 °C. The specific heat per bond is obtained by dividing the bulk specific heat by the total number of bonds involved.[72] For other usual materials, one bond represents all on average, and therefore, there is only one specific heat for the representative bond. The thermal response of all the bonds is identical, without any discrimination in responding to thermal excitation.[73]

However, for water ice, the representative O:H−O bond is composed of two segments that must have their respective specific heat. The strong disparity between the specific heat $\eta_x(T/\Theta_{Dx})$, as illustrated in Figure 4a, makes water perform

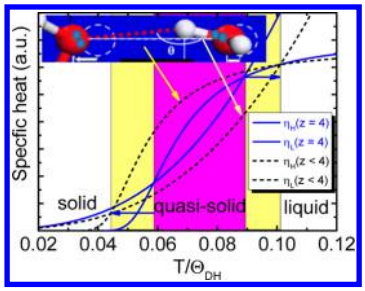

Figure 4. Superposition of the specific heat $\eta_x(T/\Theta_{Dx})$ curves yields two intersecting temperatures T_m and T_N that define the boundaries of the solid/quasisolid/liquid phase. Molecular undercoordination (z < 4) stretches $\eta_H(T/\Theta_{DH})$ by raising the $\Theta_{DH}(\omega_H)$ and depresses the $\eta_L(T/\Theta_{DL})$ by lowering the $\Theta_{DL}(\omega_L)$, which disperses the intersecting temperatures in opposite directions. Therefore, nanodroplets, nanobubbles, and water ice skins undergo simultaneously T_N depression and T_m elevation, and the extent of dispersion varies with the fraction of undercoordinated molecules of the object.[42]

differently from other normal substance with only one $\eta(T/\Theta_D)$ curve. Parameters that characterize the respective $\eta_x(T/\Theta_{Dx})$ include the Debye temperature Θ_{Dx} and the thermal integration of the $\eta_x(T/\Theta_{Dx})$. The Θ_{Dx}, which is lower than the T_{mx}, determines the rate of the $\eta_x(T/\Theta_{Dx})$ curve reaching saturation. The $\eta_x(T/\Theta_{Dx})$ curve of the segment with a relatively lower Θ_{Dx} value will rise to saturation quicker than the other segment. The Θ_{Dx} is proportional to the characteristic frequency of vibration ω_x, according to Einstein's relation: $\hbar\omega_x = k\Theta_{Dx}$, with $\hbar$ and k being constant.

On the other hand, the integral of the $\eta_x(T/\Theta_{Dx})$ curve from 0 K to the T_{mx} is proportional to the cohesive energy E_x per segment.[72] The T_{mx} is the temperature at which the vibration amplitude of an atom/molecule expands abruptly to more than 3% of its diameter irrespective of the environment or the size of a molecular cluster.[74,75] Thus, with the known values of $\omega_L \sim 200$ cm^{-1} for O:H stretching and $\omega_H \sim 3200$ cm^{-1} for H−O stretching,[13] $\Theta_{DL} = 198$ K < 273 K (T_m), $E_L = 0.095$ eV,[69] and $E_H = 3.97$ eV,[65] one can estimate $\Theta_{DH} \approx 16 \times \Theta_{DL} \approx 3200$ K and $T_{mH} \gg \Theta_{DH}$ form the H−O bond from the following:

$$\begin{cases} \Theta_{DL}/\Theta_{DH} \approx 198/\Theta_{DH} \\ \qquad\qquad \approx \omega_L/\omega_H \\ \qquad\qquad \approx 200/3200 \sim 1/16 \\ \left(\int_0^{T_{mH}} \eta_H dt\right)/\left(\int_0^{T_{mL}} \eta_L dt\right) \\ \quad \approx E_H/E_L \\ \quad \approx 4.0/0.1 \sim 40 \end{cases} \tag{10}$$

The η_L ends at $T_{mL} = 273$ K for the O:H nonbond, and the η_H ends at $T_{mH} \sim 3200$ K for the H−O bond, which means that the area covered by the η_H curve is 40 times that covered by the η_L curve.

4.3. Water Quasisolid Phase Boundary Dispersivity. Second, a superposition of these two η_x curves yields two intersecting temperatures that divide the full temperature range into phases of liquid, quasisolid, and solid with different η_L/η_H ratios (see Figure 4a). In the liquid and in the solid phase (η_L/η_H < 1), the O:H nonbond contracts more than the H−O expands at cooling, resulting in the cooling densification of water and ice.[7,14] In the quasisolid phase, the O:H and the H−O swap roles (η_H/η_L < 1): the H−O contracts less than the O:H expands at cooling, so the $\Delta d_{OO} > 0$ and water in quasisolid phase become less dense as it cools, which is responsible for ice floating.[13] At the quasisolid phase boundaries ($\eta_H/\eta_L = 1$), Δd_L and Δd_H change sign, which correspond to density extremes. Ideally, the T_m corresponds to the maximal density at 4 °C liquid and the T_N the minimal density at −15 °C for bulk water.[7,14,76]

One can imagine what will happen to the phase boundaries by raising the Θ_{DH} and meanwhile lowering the Θ_{DL}. The η_L will saturate quicker and the η_H slower than they were in the bulk standard. This process will raise the T_m and lower the T_N. With the known bulk values of $\Theta_{DL} = 198$ K, $T_m = 273$ K, $T_N = 258$ K, and the respective ω_x (in Table 3) and E_x (in Table 4) one can estimate the cluster size dependence of the Θ_{Dx}, T_m, and T_N using the following relationships[18]

$$\begin{cases} \Theta_{Dx} \propto \omega_x \\ T_{N,m} \propto E_{L,H} \end{cases}$$

Numerical reproduction of the $T_m(P)$ profiles[66] indicates that the T_m is proportional to E_H, and Figure 4a suggests that the T_N be proportional to E_L. In order to minimize calculation artifacts, a modification of the $\omega_L(N)$ curve in Figure 2b is made with respect to the measured value of 220 cm^{-1} for bulk water and to that the calculated ω_x matches the measured value at $N = 2$. This modification improves the precision of estimating cluster size dependence of the Θ_{DL}. As featured in Table 3, the estimated N-dependent T_m and T_N agree with trends of observations.

Such a phase-boundary dispersivity is responsible for the thermodynamic behavior of water droplets and gas bubbles, particularly at the nanometer scales. These systems of undercoordinated molecular dominance have far-reaching physical, chemical, and biological effects because molecular undercoordination induced unusual bond-electron−phonon behavior, as afore discussed. Water nanodroplets and nanobubbles do follow the trend of T_m elevation and T_N depression because of the dominant fraction of undercoordinated skin molecules. Droplet size reduction raises the $\Theta_{DH}(\omega_H)$ and stretches the $\eta_H(T)$ curve and, meanwhile, lowers the $\Theta_{DL}(\omega_L)$

DOI: 10.1021/acs.jpcc.5b03921
J. Phys. Chem. C 2015, 119, 16962−16971

and compresses the $\eta_L(T)$ curve, which disperses the extreme-density temperatures. A bubble is just the inversion of a droplet; a hollow sphere like a soap bubble contains two skins—the inner and the outer. Both skins are in the supersolid phase, and the volume fraction of such a supersolid phase over the entire liquid-shell volume is much greater than simply a droplet. Therefore, bubbles demonstrate more significantly the supersolidity nature—elastic, hydrophobic, and thermally stable, which makes bubbles mechanically stronger and thermally more stable.[6]

5. CONCLUSIONS

Lagrangian solution to the O:H−O bond oscillating dynamics has transformed the observed (d_x, ω_x) into the (k_x, E_x) and thus enabled probing the potential paths for the O:H−O bond relaxing with water cluster size, which is beyond the scope of other currently available approaches. Consistency between calculations and experimental observations on the O:H−O energy relaxation evidence consistently the persistence and significance of the asymmetric short-range interactions and Coulomb repulsion in the flexible, polarizable O:H−O bond and the molecular undercoordination induced O:H−O cooperative relaxation. Such an O:H−O bond cooperative relaxation in segmental length, phonon frequency, and cohesive energy disperses the quasisolid phase boundaries. H−O energy gain elevates the melting point, and O:H energy loss depresses the freezing point pertaining to water droplets and bubbles of which the undercoordinated molecules become dominant.

AUTHOR INFORMATION

Corresponding Author

*Tel.: 65 67904517. E-mail: ecqsun@ntu.edu.sg.

Author Contributions

#Authors made equal contribution. CQ was associated with honorary appointments at the rest of the affiliations.

Notes

The authors declare no competing financial interest.

ACKNOWLEDGMENTS

Financial support from National Natural Science Foundation (No. 21273191) of China is acknowledged.

REFERENCES

(1) Huang, Y.; Zhang, X.; Ma, Z.; Zhou, Y.; Zheng, W.; Zhou, J.; Sun, C. Q. Hydrogen-Bond Relaxation Dynamics: Resolving Mysteries of Water Ice. *Coord. Chem. Rev.* **2015**, *285*, 109−165.

(2) Petkov, V.; Ren, Y.; Suchomel, M. Molecular Arrangement in Water: Random but Not Quite. *J. Phys.: Condens. Matter* **2012**, *24*, 155102.

(3) Tsai, M. K.; Kuo, J. L.; Lu, J. M. The Dynamics and Spectroscopic Fingerprint of Hydroxyl Radical Generation through Water Dimer Ionization: Ab Initio Molecular Dynamic Simulation Study. *Phys. Chem. Chem. Phys.* **2012**, *14*, 13402−13408.

(4) Ostmeyer, J.; Chakrapani, S.; Pan, A. C.; Perozo, E.; Roux, B. Recovery from Slow Inactivation in K Channels Is Controlled by Water Molecules. *Nature* **2013**, *501*, 121−124.

(5) Kang, D. D.; Dai, J.; Sun, H.; Hou, Y.; Yuan, J. Quantum Similation of Thermally Driven Phase Transition and O K-Edge Absorption of High-Pressure Ice. *Sci. Rep.* **2013**, *3*, 3272.

(6) Zhang, X.; Huang, Y.; Ma, Z.; Zhou, Y.; Zheng, W.; Zhou, J.; Sun, C. Q. A Common Supersolid Skin Covering Both Water and Ice. *Phys. Chem. Chem. Phys.* **2014**, *16*, 22987−22994.

(7) Erko, M.; Wallacher, D.; Hoell, A.; Hauss, T.; Zizak, I.; Paris, O. Density Minimum of Confined Water at Low Temperatures: A Combined Study by Small-Angle Scattering of X-Rays and Neutrons. *Phys. Chem. Chem. Phys.* **2012**, *14*, 3852−3858.

(8) Lakhanpal, M. L.; Puri, B. R. Boiling Point of Capilary-Condensed Water. *Nature* **1953**, *172*, 917−917.

(9) Li, L.; Kazoe, Y.; Mawatari, K.; Sugii, Y.; Kitamori, T. Viscosity and Wetting Property of Water Confined in Extended Nanospace Simultaneously Measured from Highly-Pressurized Meniscus Motion. *J. Phys. Chem. Lett.* **2012**, *3*, 2447−2452.

(10) Qiu, H.; Guo, W. Electromelting of Confined Monolayer Ice. *Phys. Rev. Lett.* **2013**, *110*, 195701.

(11) Wang, C.; Lu, H.; Wang, Z.; Xiu, P.; Zhou, B.; Zuo, G.; Wan, R.; Hu, J.; Fang, H. Stable Liquid Water Droplet on a Water Monolayer Formed at Room Temperature on Ionic Model Substrates. *Phys. Rev. Lett.* **2009**, *103*, 137801−137804.

(12) James, M.; Darwish, T. A.; Ciampi, S.; Sylvester, S. O.; Zhang, Z. M.; Ng, A.; Gooding, J. J.; Hanley, T. L. Nanoscale Condensation of Water on Self-Assembled Monolayers. *Soft Matter* **2011**, *7*, 5309−5318.

(13) Sun, C. Q.; Zhang, X.; Fu, X.; Zheng, W.; Kuo, J.-l.; Zhou, Y.; Shen, Z.; Zhou, J. Density and Phonon-Stiffness Anomalies of Water and Ice in the Full Temperature Range. *J. Phys. Chem. Lett.* **2013**, *4*, 3238−3244.

(14) Mallamace, F.; Branca, C.; Broccio, M.; Corsaro, C.; Mou, C. Y.; Chen, S. H. The Anomalous Behavior of the Density of Water in the Range 30 K < T < 373 K. *Proc. Natl. Acad. Sci. U. S. A.* **2007**, *104*, 18387−18391.

(15) Alabarse, F. G.; Haines, J.; Cambon, O.; Levelut, C.; Bourgogne, D.; Haidoux, A.; Granier, D.; Coasne, B. Freezing of Water Confined at the Nanoscale. *Phys. Rev. Lett.* **2012**, *109*, 035701.

(16) Moro, R.; Rabinovitch, R.; Xia, C.; Kresin, V. V. Electric Dipole Moments of Water Clusters from a Beam Deflection Measurement. *Phys. Rev. Lett.* **2006**, *97*, 123401.

(17) Wilson, K. R.; Schaller, R. D.; Co, D. T.; Saykally, R. J.; Rude, B. S.; Catalano, T.; Bozek, J. D. Surface Relaxation in Liquid Water and Methanol Studied by X-Ray Absorption Spectroscopy. *J. Chem. Phys.* **2002**, *117*, 7738−7744.

(18) Sun, C. Q. *Relaxation of the Chemical Bond*; Springer: Heidelberg, 2014; Vol. *108*.

(19) Bergmann, U.; Di Cicco, A.; Wernet, P.; Principi, E.; Glatzel, P.; Nilsson, A. Nearest-Neighbor Oxygen Distances in Liquid Water and Ice Observed by X-Ray Raman Based Extended X-Ray Absorption Fine Structure. *J. Chem. Phys.* **2007**, *127*, 174504.

(20) Wilson, K. R.; Rude, B. S.; Catalano, T.; Schaller, R. D.; Tobin, J. G.; Co, D. T.; Saykally, R. J. X-Ray Spectroscopy of Liquid Water Microjets. *J. Phys. Chem. B* **2001**, *105*, 3346−3349.

(21) Solveyra, E. G.; de la Llave, E.; Molinero, V.; Soler-Illia, G.; Scherlis, D. A. Structure, Dynamics, and Phase Behavior of Water in Tio2 Nanopores. *J. Phys. Chem. C* **2013**, *117*, 3330−3342.

(22) Huang, Y.; Zhang, X.; Ma, Z.; Zhou, Y.; Zhou, J.; Zheng, W.; Sun, C. Q. Size, Separation, Structure Order, and Mass Density of Molecules Packing in Water and Ice. *Sci. Rep.* **2013**, *3*, 3005.

(23) Hammer, N. I.; Shin, J. W.; Headrick, J. M.; Diken, E. G.; Roscioli, J. R.; Weddle, G. H.; Johnson, M. A. How Do Small Water Clusters Bind an Excess Electron? *Science* **2004**, *306*, 675−679.

(24) Siefermann, K. R.; Liu, Y.; Lugovoy, E.; Link, O.; Faubel, M.; Buck, U.; Winter, B.; Abel, B. Binding Energies, Lifetimes and Implications of Bulk and Interface Solvated Electrons in Water. *Nat. Chem.* **2010**, *2*, 274−279.

(25) Verlet, J. R. R.; Bragg, A. E.; Kammrath, A.; Cheshnovsky, O.; Neumark, D. M. Observation of Large Water-Cluster Anions with Surface-Bound Excess Electrons. *Science* **2005**, *307*, 93−96.

(26) Vacha, R.; Marsalek, O.; Willard, A. P.; Bonthuis, D. J.; Netz, R. R.; Jungwirth, P. Charge Transfer between Water Molecules as the Possible Origin of the Observed Charging at the Surface of Pure Water. *J. Phys. Chem. Lett.* **2012**, *3*, 107−111.

(27) Marsalek, O.; Uhlig, F.; Frigato, T.; Schmidt, B.; Jungwirth, P. Dynamics of Electron Localization in Warm Versus Cold Water Clusters. *Phys. Rev. Lett.* **2010**, *105*, 043002.

DOI: 10.1021/acs.jpcc.5b03921
J. Phys. Chem. C 2015, 119, 16962−16971

(28) Baletto, F.; Cavazzoni, C.; Scandolo, S. Surface Trapped Excess Electrons on Ice. *Phys. Rev. Lett.* **2005**, *95*, 176801.
(29) Turi, L.; Sheu, W. S.; Rossky, P. J. Characterization of Excess Electrons in Water-Cluster Anions by Quantum Simulations. *Science* **2005**, *309*, 914−917.
(30) Abu-Samha, M.; Borve, K. J.; Winkler, M.; Harnes, J.; Saethre, L. J.; Lindblad, A.; Bergersen, H.; Ohrwall, G.; Bjorneholm, O.; Svensson, S. The Local Structure of Small Water Clusters: Imprints on the Core-Level Photoelectron Spectrum. *J. Phys. B: At., Mol. Opt. Phys.* **2009**, *42*, 055201.
(31) Nishizawa, K.; Kurahashi, N.; Sekiguchi, K.; Mizuno, T.; Ogi, Y.; Horio, T.; Oura, M.; Kosugi, N.; Suzuki, T. High-Resolution Soft X-Ray Photoelectron Spectroscopy of Liquid Water. *Phys. Chem. Chem. Phys.* **2011**, *13*, 413−417.
(32) Winter, B.; Aziz, E. F.; Hergenhahn, U.; Faubel, M.; Hertel, I. V. Hydrogen Bonds in Liquid Water Studied by Photoelectron Spectroscopy. *J. Chem. Phys.* **2007**, *126*, 124504.
(33) Buck, U.; Huisken, F. Infrared Spectroscopy of Size-Selected Water and Methanol Clusters. *Chem. Rev.* **2000**, *100*, 3863−3890.
(34) Otto, K. E.; Xue, Z.; Zielke, P.; Suhm, M. A. The Raman Spectrum of Isolated Water Clusters. *Phys. Chem. Chem. Phys.* **2014**, *16*, 9849.
(35) Kahan, T. F.; Reid, J. P.; Donaldson, D. J. Spectroscopic Probes of the Quasi-Liquid Layer on Ice. *J. Phys. Chem. A* **2007**, *111*, 11006−11012.
(36) Ceponkus, J.; Uvdal, P.; Nelander, B. Water Tetramer, Pentamer, and Hexamer in Inert Matrices. *J. Phys. Chem. A* **2012**, *116*, 4842−4850.
(37) Sun, Q. The Raman Oh Stretching Bands of Liquid Water. *Vib. Spectrosc.* **2009**, *51*, 213−217.
(38) Hirabayashi, S.; Yamada, K. M. T. Infrared Spectra and Structure of Water Clusters Trapped in Argon and Krypton Matrices. *J. Mol. Struct.* **2006**, *795*, 78−83.
(39) Shen, Y. R.; Ostroverkhov, V. Sum-Frequency Vibrational Spectroscopy on Water Interfaces: Polar Orientation of Water Molecules at Interfaces. *Chem. Rev.* **2006**, *106*, 1140−1154.
(40) Buch, V.; Bauerecker, S.; Devlin, J. P.; Buck, U.; Kazimirski, J. K. Solid Water Clusters in the Size Range of Tens-Thousands of H2o: A Combined Computational/Spectroscopic Outlook. *Int. Rev. Phys. Chem.* **2004**, *23*, 375−433.
(41) Cross, P. C.; Burnham, J.; Leighton, P. A. The Raman Spectrum and the Structure of Water. *J. Am. Chem. Soc.* **1937**, *59*, 1134−1147.
(42) Zhang, X.; Sun, P.; Huang, Y.; Ma, Z.; Liu, X.; Zhou, J.; Zheng, W.; Sun, C. Q. Water Nanodroplet Thermodynamics: Quasi-Solid Phase-Boundary Dispersivity. *J. Phys. Chem. B* **2015**, *119*, 5265−5269.
(43) Tyrrell, J. W.; Attard, P. Images of Nanobubbles on Hydrophobic Surfaces and Their Interactions. *Phys. Rev. Lett.* **2001**, *87*, 176104.
(44) Teixeira, J. High-Pressure Physics - the Double Identity of Ice X. *Nature* **1998**, *392*, 232−233.
(45) Pauling, L. The Structure and Entropy of Ice and of Other Crystals with Some Randomness of Atomic Arrangement. *J. Am. Chem. Soc.* **1935**, *57*, 2680−2684.
(46) Wernet, P.; Nordlund, D.; Bergmann, U.; Cavalleri, M.; Odelius, M.; Ogasawara, H.; Naslund, L. A.; Hirsch, T. K.; Ojamae, L.; Glatzel, P. The Structure of the First Coordination Shell in Liquid Water. *Science* **2004**, *304*, 995−999.
(47) Soper, A. K. An Asymmetric Model for Water Structure. *J. Phys.: Condens. Matter* **2005**, *17*, S3273−S3282.
(48) Wikfeldt, K. T.; Leetmaa, M.; Ljungberg, M. P.; Nilsson, A.; Pettersson, L. G. M. On the Range of Water Structure Models Compatible with X-Ray and Neutron Diffraction Data. *J. Phys. Chem. B* **2009**, *113*, 6246−6255.
(49) Leetmaa, M.; Wikfeldt, K. T.; Ljungberg, M. P.; Odelius, M.; Swenson, J.; Nilsson, A.; Pettersson, L. G. M. Diffraction and Ir/Raman Data Do Not Prove Tetrahedral Water. *J. Chem. Phys.* **2008**, *129*, 084502.
(50) Nilsson, A.; Pettersson, L. G. M. Perspective on the Structure of Liquid Water. *Chem. Phys.* **2011**, *389*, 1−34.
(51) Kuhne, T. D.; Khaliullin, R. Z. Electronic Signature of the Instantaneous Asymmetry in the First Coordination Shell of Liquid Water. *Nat. Commun.* **2013**, *4*, 1450.
(52) Kumagai, N.; Kawamura, K.; Yokokawa, T. An Interatomic Potential Model for H2o: Applications to Water and Ice Polymorphs. *Mol. Simul.* **1994**, *12*, 177−186.
(53) Zhang, J.; Chen, P.; Yuan, B.; Ji, W.; Cheng, Z.; Qiu, X. Real-Space Identification of Intermolecular Bonding with Atomic Force Microscopy. *Science* **2013**, *342*, 611−614.
(54) Guo, J.; Meng, X.; Chen, J.; Peng, J.; Sheng, J.; Li, X.-Z.; Xu, L.; Shi, J.-R.; Wang, E.; Jiang, Y. Real-Space Imaging of Interfacial Water with Submolecular Resolution. *Nat. Mater.* **2014**, *13*, 184−189.
(55) Wang, B.; Xin, M.; Dai, X.; Song, R.; Meng, Y.; Han, J.; Jiang, W.; Wang, Z.; Zhang, R. Electronic Delocalization in Small Water Rings. *Phys. Chem. Chem. Phys.* **2015**, *17*, 2987−2990.
(56) Li, J. Inelastic Neutron Scattering Studies of Hydrogen Bonding in Ices. *J. Chem. Phys.* **1996**, *105*, 6733−6755.
(57) Kolesnikov, A.; Li, J.; Parker, S.; Eccleston, R.; Loong, C.-K. Vibrational Dynamics of Amorphous Ice. *Phys. Rev. B: Condens. Matter Mater. Phys.* **1999**, *59*, 3569.
(58) Li, J.; Ross, D. Evidence for Two Kinds of Hydrogen Bond in Ice. *Nature* **1993**, *365*, 327−329.
(59) Ortmann, F.; Bechstedt, F.; Schmidt, W. G. Semiempirical Van Der Waals Correction to the Density Functional Description of Solids and Molecular Structures. *Phys. Rev. B: Condens. Matter Mater. Phys.* **2006**, *73*, 205101.
(60) Sun, H. Compass: An Ab Initio Force-Field Optimized for Condensed-Phase Applicationsoverview with Details on Alkane and Benzene Compounds. *J. Phys. Chem. B* **1998**, *102*, 7338−7364.
(61) Sun, C. Q.; Zhang, X.; Zheng, W. T. Hidden Force Opposing Ice Compression. *Chem. Sci.* **2012**, *3*, 1455−1460.
(62) Huang, Y.; Zhang, X.; Ma, Z.; Zhou, Y.; Zhou, G.; Sun, C. Q. Hydrogen-Bond Asymmetric Local Potentials in Compressed Ice. *J. Phys. Chem. B* **2013**, *117*, 13639−13645.
(63) Zhang, X.; Huang, Y.; Ma, Z.; Zhou, Y.; Zhou, J.; Zheng, W.; Jiang, Q.; Sun, C. Q. Hydrogen-Bond Memory and Water-Skin Supersolidity Resolving the Mpemba Paradox. *Phys. Chem. Chem. Phys.* **2014**, *16*, 22995−23002.
(64) Zhang, X.; Yan, T.; Huang, Y.; Ma, Z.; Liu, X.; Zou, B.; Sun, C. Q. Mediating Relaxation and Polarization of Hydrogen-Bonds in Water by Nacl Salting and Heating. *Phys. Chem. Chem. Phys.* **2014**, *16*, 24666−24671.
(65) Sun, C. Q.; Zhang, X.; Zhou, J.; Huang, Y.; Zhou, Y.; Zheng, W. Density, Elasticity, and Stability Anomalies of Water Molecules with Fewer Than Four Neighbors. *J. Phys. Chem. Lett.* **2013**, *4*, 2565−2570.
(66) Zhang, X.; Sun, P.; Huang, Y.; Yan, T.; Ma, Z.; Liu, X.; Zou, B.; Zhou, J.; Zheng, W.; Sun, C. Q. Water's Phase Diagram: From the Notion of Thermodynamics to Hydrogen-Bond Cooperativity. *Prog. Solid State Chem.* **2015**, DOI: 10.1016/j.progsolidstchem.2015.03.001.
(67) Liu, Y.; Wu, J. Communication: Long-Range Angular Correlations in Liquid Water. *J. Chem. Phys.* **2013**, *139*, 041103.
(68) Li, X. Z.; Walker, B.; Michaelides, A. Quantum Nature of the Hydrogen Bond. *Proc. Natl. Acad. Sci. U. S. A.* **2011**, *108*, 6369−6373.
(69) Zhao, M.; Zheng, W. T.; Li, J. C.; Wen, Z.; Gu, M. X.; Sun, C. Q. Atomistic Origin, Temperature Dependence, and Responsibilities of Surface Energetics: An Extended Broken-Bond Rule. *Phys. Rev. B: Condens. Matter Mater. Phys.* **2007**, *75*, 085427.
(70) Harich, S. A.; Hwang, D. W. H.; Yang, X.; Lin, J. J.; Yang, X.; Dixon, R. N. Photodissociation of H2o at 121.6 Nm: A State-to-State Dynamical Picture. *J. Chem. Phys.* **2000**, *113*, 10073−10090.
(71) Debenedetti, P. G.; Stanley, H. E. Supercooled and Glassy Water. *Phys. Today* **2003**, *56*, 40−46.
(72) Sun, C. Q. Thermo-Mechanical Behavior of Low-Dimensional Systems: The Local Bond Average Approach. *Prog. Mater. Sci.* **2009**, *54*, 179−307.
(73) Gu, M. X.; Zhou, Y. C.; Sun, C. Q. Local Bond Average for the Thermally Induced Lattice Expansion. *J. Phys. Chem. B* **2008**, *112*, 7992−7995.

DOI: 10.1021/acs.jpcc.5b03921
J. Phys. Chem. C 2015, 119, 16962−16971

(74) Omar, M. A. *Elementary Solid State Physics: Principles and Applications*; Addison-Wesley: New York, 1993.
(75) Lindemann, F. A. The Calculation of Molecular Natural Frequencies. *Phys. Z.* **1910**, *11*, 609−612.
(76) Moore, E. B.; Molinero, V. Structural Transformation in Supercooled Water Controls the Crystallization Rate of Ice. *Nature* **2011**, *479*, 506−508.

DOI: 10.1021/acs.jpcc.5b03921
J. Phys. Chem. C 2015, 119, 16962−16971